Published in Journal of Quantitative Spectroscopy and Radiative Transfer 221 (2018) 286 - 299

Co-Polarized and Cross-Polarized Scattering of an Off-Axis Focused Gaussian Beam by a Spherical Particle. 3. Diffraction, the Debye Series, and Time-Domain Scattering

Philip Laven[1] and James A. Lock[2,*]
[1]9 Russells Crescent, Horley RH6 7DJ, UK
[2]Physics Dept., Cleveland State University, Cleveland, OH 44115, USA
[*]Corresponding author. *E-mail address:* j.lock@csuohio.edu

Abstract
Diffraction in the near-forward direction is examined for the localized model of an off-axis focused Gaussian beam scattered by a sphere when the beam is translated off-axis either in the scattering plane or perpendicular to it. The results are analyzed using the Fraunhofer diffraction approximation. We also obtain various Debye series contributions to the exact GLMT co-polarized VV and HH scattering amplitudes and cross-polarized VH and HV scattering amplitudes, and discuss their interpretation. Time-domain scattering is also considered for both the exact GLMT scattering amplitudes and our approximation to them, for which the sum over azimuthal modes is evaluated analytically. It is found that although the approximation accurately reproduces the overall magnitude of the scattered intensity, it is not as accurate in reproducing the phase of high-frequency oscillations in the intensity.

Key words: Mie theory, generalize Lorenz-Mie theory, polarization-resolved scattering, cross-polarized scattering, diffraction, time-domain scattering.

1. Introduction

This contribution is the third and final installment in our study of polarization-resolved scattering of an off-axis Gaussian beam by a single homogeneous dielectric spherical particle [1,2]. A far-zone detector array is located in the horizontal scattering plane which contains the center of the sphere. The polarization direction at the center of the incident beam's focal waist is either vertical, V, or horizontal, H. Similarly, a polarizing filter placed in front of the detectors passes either vertically polarized scattered light, V, or horizontally polarized light, H. We have previously shown that only VV and HH co-polarized scattering occur if the incident beam is a plane wave, an on-axis Gaussian beam, or a Gaussian beam translated off-axis in the scattering plane. But if an incident Gaussian beam is translated off-axis perpendicular to the scattering plane, VH and HV cross-polarized scattering occur in addition to co-polarized scattering.

Using the localized model of a mildly-focused off-axis Gaussian beam, the exact generalized Lorenz-Mie theory (GLMT) polarization-resolved scattering amplitudes, $S_{VV}(\theta,\varphi)$, $S_{VH}(\theta,\varphi)$, $S_{HV}(\theta,\varphi)$, $S_{HH}(\theta,\varphi)$, were obtained in [1]. They contain a sum over partial waves n and azimuthal modes m. In [2] we obtained an accurate approximation to the scattering amplitudes in the large particle and moderately focused beam limit for which the sum over azimuthal

modes can be evaluated analytically. In this manuscript we investigate additional features of polarization-resolved scattering, both in the frequency-domain and in the time-domain.

The body of the manuscript proceeds as follows. In Sec.2, for convenience, we repeat the results of [1,2] that will be used here. In Sec. 3 we examine diffraction for near-forward scattering, and analyze the differences in the diffraction signature when the incident beam is translated off-axis in the scattering plane and perpendicular to it. Our analysis is based on the close analogy between GLMT-Debye-series diffraction by a sphere and Fraunhofer diffraction by a circular obstacle [3,4]. In Sec.4 we comment on the principal features of the p=0,1,2,3 terms of the Debye series expansion of the exact GLMT scattering amplitudes, corresponding to diffraction-plus-external reflection of the partial waves, transmission, and transmission following one or two internal reflections. In Sec.5, we compute time-domain scattering for both the exact GLMT scattering amplitudes, and for our approximation to them. We find that although the time-domain signature of the exact GLMT scattering amplitudes behaves as expected, the time-domain signature of our approximation contains a number of artifacts and distortions. This is because our approximation renders the overall magnitude of the scattered intensity correctly, but fails to faithfully reproduce the phase of high-frequency oscillations in the intensity. Lastly, our final conclusions are stated in Sec.6.

2. Off-Axis Scattering by a Focused Gaussian Beam

The incident Gaussian beam has peak electric field strength E_0, wavelength λ, wave number $k=2\pi/\lambda$, angular frequency ω, implicit time dependence $\exp(-i\omega t)$, and confinement parameter

$$s = \lambda/(2\pi w_0) \quad . \tag{1}$$

The beam's electric field half-width is w_0, and the center of the beam's focal waist is located at (ρ_0,φ_0) in the z=0 plane whose origin coincides with the center of the scattering particle. The homogeneous spherical particle has radius a and refractive index M. The $r\to\infty$ far-zone scattered electric and magnetic fields are

$$\mathbf{E_{scatt}}(r,\theta,\varphi) = (iE_0/kr)\exp(ikr)\,[S_2(\theta,\varphi)\,\mathbf{u_\theta} - S_1(\theta,\varphi)\,\mathbf{u_\varphi}] \tag{2a}$$

$$\mathbf{B_{scatt}}(r,\theta,\varphi) = (iE_0/ckr)\exp(ikr)\,[S_1(\theta,\varphi)\,\mathbf{u_\theta} + S_2(\theta,\varphi)\,\mathbf{u_\varphi}] \quad , \tag{2b}$$

where φ is the azimuthal angle of the scattering plane with respect to the xz plane, θ is the scattering angle in that plane, and c is the speed of light. If the electric field of the localized model of an incident Gaussian beam is x-polarized at the center of its focal waist, the far-zone GLMT scattering amplitudes are [1]

$$S_1(\theta,\varphi;\rho_0,\varphi_0) = i\sum_{n=1}^{\infty} c_n F_n (n+1/2)\, b_n\, I_1(Q_n)\, \tau_n^0(\theta)\, \sin(\varphi_0)$$

$$+ i\sum_{n=1}^{\infty} c_n F_n (n+1/2)\, b_n \sum_{m=1}^{n} [-i/(n+1/2)]^m\, \tau_n^m(\theta) \times [I_m^-(Q_n)\sin(m\chi)\cos(\varphi_0) + I_m^+(Q_n)\cos(m\chi)\sin(\varphi_0)]$$

$$+ \mathrm{i} \sum_{n=1}^{\infty} c_n F_n (n+1/2)\, a_n \sum_{m=1}^{n} [-\mathrm{i}/(n+1/2)]^m\, m\pi_n^m(\theta) \times [\, \mathrm{I}_m^+(Q_n) \sin(m\chi) \cos(\varphi_0) + \mathrm{I}_m^-(Q_n) \cos(m\chi) \sin(\varphi_0)] \qquad (3a)$$

and

$$S_2(\theta,\varphi;\rho_0,\varphi_0) = \mathrm{i} \sum_{n=1}^{\infty} c_n F_n (n+1/2)\, a_n \mathrm{I}_1(Q_n)\, \tau_n^0(\theta) \cos(\varphi_0)$$

$$+ \mathrm{i} \sum_{n=1}^{\infty} c_n F_n (n+1/2)\, a_n \sum_{m=1}^{n} [-\mathrm{i}/(n+1/2)]^m\, \tau_n^m(\theta) \times [\mathrm{I}_m^+(Q_n) \cos(m\chi) \cos(\varphi_0) - \mathrm{I}_m^-(Q_n) \sin(m\chi) \sin(\varphi_0)]$$

$$+ \mathrm{i} \sum_{n=1}^{\infty} c_n F_n (n+1/2)\, b_n \sum_{m=1}^{n} [-\mathrm{i}/(n+1/2)]^m\, m\pi_n^m(\theta) \times [\mathrm{I}_m^-(Q_n) \cos(m\chi) \cos(\varphi_0) - \mathrm{I}_m^+(Q_n) \sin(m\chi) \sin(\varphi_0)] \ , \qquad (3b)$$

where

$$c_n \equiv (2n+1)/[n(n+1)] \qquad (4a)$$

$$F_n \equiv \exp(-\rho_0^2/w_0^2) \exp[-s^2 (n+1/2)^2] \qquad (4b)$$

$$Q_n \equiv (n+1/2)\, \varepsilon \qquad (4c)$$

$$\varepsilon \equiv 2s\rho_0/w_0 \qquad (4d)$$

$$\chi \equiv \varphi - \varphi_0 \ , \qquad (4e)$$

$$\mathrm{I}_m^{\pm}(Q_n) \equiv \mathrm{I}_{m-1}(Q_n) \pm \mathrm{I}_{m+1}(Q_n) \ , \qquad (4f)$$

$\mathrm{I}_m(Q_n)$ is a modified Bessel function, and a_n and b_n are the transverse magnetic (TM) and transverse electric (TE) partial wave scattering amplitudes of Lorenz-Mie theory, respectively. If the electric field of the incident Gaussian beam is instead *y*-polarized at the center of its focal waist, S_2 is identical to S_1 for an *x*-polarized beam with a_n and b_n interchanged, and S_1 is the negative of S_2 for an *x*-polarized beam with a_n and b_n interchanged. When the incident beam is polarized in the vertical *x* direction and the scattering plane is the horizontal *yz* plane with $\varphi=\pm 90°$, the VV scattering amplitude is $S_1(\theta,\varphi;\rho_0,\varphi_0)$ and the VH scattering amplitude is $S_2(\theta,\varphi;\rho_0,\varphi_0)$. When the incident beam is polarized in the horizontal *y* direction, the HV scattering amplitude is $S_1(\theta,\varphi;\rho_0,\varphi_0)$ and the HH scattering amplitude is $S_2(\theta,\varphi;\rho_0,\varphi_0)$.

In [2] we developed an accurate transitional approximation for $0° \ll \theta \ll 180°$ to the co-polarized and cross-polarized scattering amplitudes of Eqs.(3a),(3b) if the particle is large, $2\pi a/\lambda \gg 1$, and the beam is mildly focused, $s \ll 1$. When the beam is translated off-axis in the $\varphi_0=-90°$ direction in the $\varphi=90°$ horizontal scattering plane, the scattering amplitudes were found to be approximately

$$S_{VV}(\theta;\rho_0) \approx \sum_{n=1}^{\infty} c_n F_n b_n \{\cosh(Q_n) [B_0 + B_2 (1 - Q_n^2) - \mathrm{i}\, A_2 Q_n] - \mathrm{i} \sinh(Q_n) [A_0 + A_2 (1 - Q_n^2) + \mathrm{i}\, B_2 Q_n]\}$$

$$+ \sum c_n F_n a_n [\cosh(Q_n) D_1 - \mathrm{i} \sinh(Q_n) C_1] \qquad (5)$$

and $S_{HH}(\theta;\rho_0)$ was obtained from Eq.(5) by interchanging a_n and b_n, where

$$A_0 = - \Pi_n(\theta)\, N_n(\theta) - (3/8)\cos(\theta)\, T_n(\theta)/N_n(\theta) - (1/8)\sin(\theta)\, \Pi_n(\theta) \quad (6a)$$

$$B_0 = T_n(\theta) - (3/8)\cos(\theta)\, \Pi_n(\theta) + (1/8)\sin(\theta)\, T_n(\theta)/N_n(\theta) \quad (6b)$$

$$C_1 = T_n(\theta)/N_n(\theta) \quad (6c)$$

$$D_1 = \Pi_n(\theta) \quad (6d)$$

$$A_2 = - (1/2)\cos(\theta)\, T_n(\theta)/N_n(\theta) \quad (6e)$$

$$B_2 = - (1/2)\cos(\theta)\, \Pi_n(\theta) \quad . \quad (6f)$$

The angular functions in Eqs.(6a)-(6f) are

$$\Pi_n(\theta) \equiv [1/\sin(\theta)]\, \{2(n+1/2) / [\pi \sin(\theta)]\}^{1/2} \sin[(n+1/2)\theta - \pi/4] \quad (7a)$$

$$T_n(\theta) \equiv (n+1/2)\{2(n+1/2) / [\pi \sin(\theta)]\}^{1/2} \cos[(n+1/2)\theta - \pi/4] \, . \quad (7b)$$

The cross-polarized scattering amplitudes $S_{VH}(\theta;\rho_0)$ and $S_{HV}(\theta;\rho_0)$ were identically zero.

If the beam is translated off-axis in the φ_0=180° direction perpendicular to the horizontal φ=90° scattering plane, the co-polarized scattering amplitudes were found to be approximately

$$S_{VV}(\theta;\rho_0) \approx \sum_{n=1}^{\infty} c_n\, F_n\, \{b_n\, [B_0 + B_2\, (1 - Q_n^{\,2})] + a_n\, D_1\} \, , \quad (8)$$

and $S_{HH}(\theta;\rho_0)$ was obtained from Eq.(8) by interchanging a_n and b_n. The cross-polarized scattering amplitudes were

$$S_{VH}(\theta;\rho_0) \approx -\mathrm{i} \sum_{n=1}^{\infty} c_n\, F_n\, Q_n\, [a_n \cos(\theta) - b_n]\, T_n(\theta)/N_n(\theta) \quad (9a)$$

$$S_{HV}(\theta;\rho_0) \approx \; - \mathrm{i} \sum_{n=1}^{\infty} c_n\, F_n\, Q_n\, [a_n - b_n \cos(\theta)]\, T_n(\theta)/N_n(\theta) \quad . \quad (9b)$$

The dominant contribution to the co-polarized scattering amplitudes of Eq.(8) using only $B_0=T_n(\theta)$, is related to the cross-polarized scattering amplitudes of Eqs.(9a),(9b) by

$$S_{VH}(\theta;\rho_0,\varphi_0) \approx -\mathrm{i}\varepsilon \cos(\varphi_0)\, [\, S_{VV}(\theta) - S_{HH}(\theta)\cos(\theta)] \,/\, \sin(\theta) \quad (10a)$$

$$S_{HV}(\theta;\rho_0,\varphi_0) \approx -\mathrm{i}\varepsilon \cos(\varphi_0)\, [S_{VV}(\theta)\cos(\theta) - S_{HH}(\theta)] \,/\, \sin(\theta) \quad . \quad (10b)$$

Another accurate transitional approximation to the far-zone scattered electric field in the near-forward direction, θ~0°, was derived in [2] for a particle with $2\pi a/\lambda \gg 1$, and a beam with $s \ll 1$. For an x-polarized incident Gaussian beam translated off-axis in an arbitrary direction, we found that

$$\mathbf{E_{scatt}}(r,\theta,\varphi;\rho_0,\varphi_0) \approx [\mathrm{i}E_0/(kr)]\, \exp(\mathrm{i}kr) \sum_{n=1}^{\infty} F_n\, (n+1/2) \times \{(a_n + b_n)\, \mathrm{J}_0(A_n) - (a_n - b_n)\, \mathrm{J}_2(A_n)\, [X \cos(2\varphi_0) + Y \sin(2\varphi_0)]\}\, \mathbf{u_x}$$

$$+ [\mathrm{i}E_0/(kr)]\, \exp(\mathrm{i}kr) \sum_{n=1}^{\infty} F_n\, (n+1/2) \times (a_n - b_n)\, \mathrm{J}_2(A_n)\, [Y \cos(2\varphi_0) - X \sin(2\varphi_0)]\, \mathbf{u_y} \quad . \quad (11)$$

The x component of Eq.(11) is $\mathbf{E_{VV}}$ and the y component is $\mathbf{E_{VH}}$. Similarly, for a y-polarized incident Gaussian beam translated off-axis in an arbitrary direction, we found that

$$\mathbf{E_{scatt}}(r,\theta,\varphi;\rho_0,\varphi_0) \approx [\mathrm{i}E_0/(kr)] \exp(\mathrm{i}kr) \sum_{n=1}^{\infty} F_n\,(n+1/2)$$

$$\times (a_n - b_n)\, \mathrm{J}_2(A_n)\, [Y \cos(2\varphi_0) - X \sin(2\varphi_0)]\, \mathbf{u_x}$$

$$+ [\mathrm{i}E_0/(kr)] \exp(\mathrm{i}kr) \sum_{n=1}^{\infty} F_n\,(n+1/2)$$

$$\times\{(a_n + b_n)\, \mathrm{J}_0(A_n) + (a_n - b_n)\, \mathrm{J}_2(A_n)\, [X \cos(2\varphi_0) + Y \sin(2\varphi_0)]\}\, \mathbf{u_y}\ . \quad (12)$$

The x component of Eq.(12) is $\mathbf{E_{HV}}$ and the y component is $\mathbf{E_{HH}}$. For off-axis incidence in the φ_0=-90° direction in the horizontal scattering plane, now given by φ=±90° and θ≥0°,

$$A_n = (n+1/2)\, (\mathrm{i}\varepsilon \mp \theta) \quad (13a)$$

$$X = 1 \quad (13b)$$

$$Y = 0\ . \quad (13c)$$

For off-axis incidence in the φ_0=180° direction perpendicular to the horizontal scattering plane, again given by φ=±90° and θ≥0°,

$$A_n = (n+1/2)\, (\theta^2 - \varepsilon^2)^{1/2} \quad (14a)$$

$$X = -(\theta^2 + \varepsilon^2)\, /\, (\theta^2 - \varepsilon^2) \quad (14b)$$

$$Y = \pm\, 2\mathrm{i}\, \theta\varepsilon\, /\, (\theta^2 - \varepsilon^2)\ . \quad (14c)$$

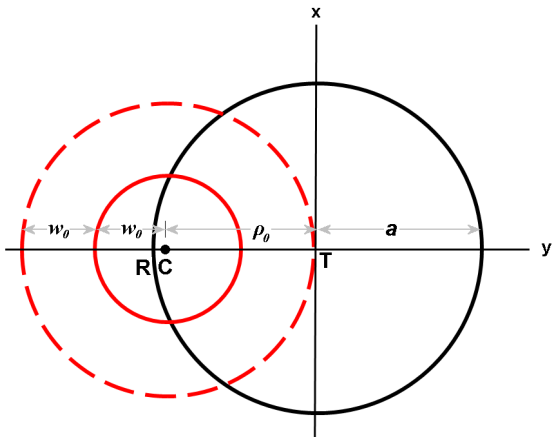

(a)

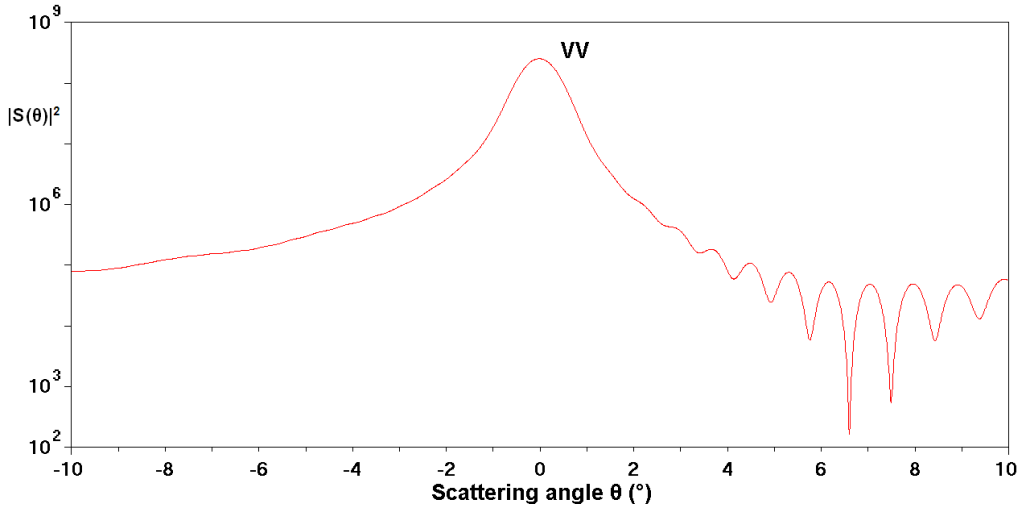

(b)

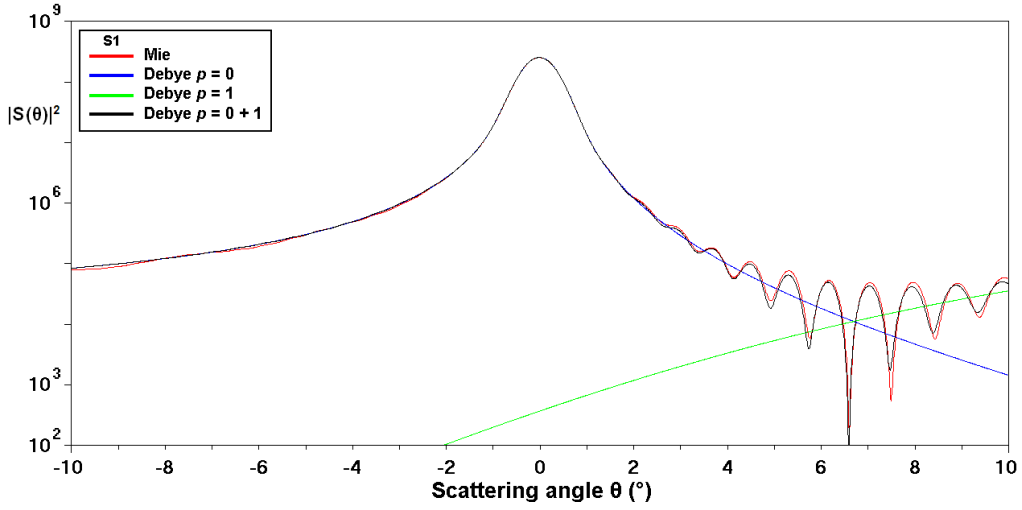

(c)

Fig.1. (a) A Gaussian beam of electric field half-width w_0 incident off-axis in the horizontal scattering plane at ρ_0, φ_0=-90° on a spherical particle of radius a. The center of the beam is at C. Near-forward transmitted rays are incident at T, and near-forward externally reflected rays are incident at R. (b) Near-forward exact GLMT scattered intensity of Eq.(3a) for off-axis incidence in the φ=90° scattering plane as a function of the scattering angle θ in the VV channel for λ=0.5145μm, w_0=20μm, ρ_0=40μm, φ_0=-90°, a=43.3μm, and M=1.33. (c) The intensity of (b) along with that of the p=0,1 terms of the Debye series decomposition of the VV scattering amplitude.

3. The Role of Diffraction

Figure 1a shows the geometry of a Gaussian beam with λ=0.5145μm, w_0=20μm that is translated off-axis with ρ_0=40μm, φ_0=-90° in the horizontal scattering plane, and is incident on a spherical particle with a=43.3μm, M=1.33 whose center is at the origin of coordinates. The figure's point of view is that of an observer on the $-z$ axis looking at both the beam and particle in the xy plane. Figure 1b gives the exact co-polarized GLMT scattered intensity of Eq.(3a) in the VV channel for -10°≤θ≤10° in the horizontal φ=90° scattering plane, and is an enlarged version of the small-θ region in Fig.2 of [1]. The strong intensity peak centered on θ=0° is due to the azimuthal focusing produced by diffraction, and scaling as a^2 rather than as a which is characteristic of geometrical optics. In ray theory, rays incident on the sphere equator in the horizontal scattering plane are transmitted through and reflected by the sphere in the same scattering plane, while rays incident in other planes of incidence, φ, remain in those other planes after interacting with the sphere. Thus in the context of ray theory, the falloff of the intensity in Fig.1b for negative θ is due to the combination of diffraction and near-forward externally reflected rays incident in the horizontal scattering plane at y_0≈-a, denoted by R in Fig.1a, and having intensity

$$I^{ray}_{p=0} \approx \exp[-2\,|\boldsymbol{\rho}-\boldsymbol{\rho}_0|^2/w_0^2] = \exp[-2\,(43.3-40.0)^2/(20.0)^2] = 0.947 \qquad (15)$$

with respect to the axial ray of unit intensity. The oscillatory structure for positive θ is due to interference of diffraction with the much weaker directly transmitted rays incident in the horizontal scattering plane at small negative y_0, denoted by T in Fig.1a, and having intensity

$$I^{ray}_{p=1} \approx \exp[-2\,|\boldsymbol{\rho}-\boldsymbol{\rho}_0|^2/w_0^2] = \exp[-2\,(40.0)^2/(20.0)^2] = 3.35\times10^{-4} \quad . \qquad (16)$$

This interpretation is reinforced by the Debye series calculation shown in Fig.1c.

Figure 2a shows the geometry of the same beam and particle, but with the beam now incident off-axis with ρ_0=40μm, φ_0=180° perpendicular to the horizontal scattering plane. Figure 2b gives the exact GLMT scattered intensity of Eqs.(3a),(3b) in the co-polarized VV and cross-polarized VH channels for -10°≤θ≤10° in the horizontal scattering plane, and is an enlarged version of the small-θ region in Fig.4 of [1]. The strong central diffraction peak rises six orders of magnitude above the near-constant background provided by the weak directly transmitted rays incident in the scattering plane at small y_0, denoted by T in Fig.2a, and having the intensity of Eq.(16). The contribution of the much weaker near-forward externally reflected rays that are incident at y_0≈±a, denoted by R in Fig.2a, and having intensity

$$I^{ray}_{p=0} \approx \exp[-2\,|\boldsymbol{\rho}-\boldsymbol{\rho}_0|^2/w_0^2] = \exp\{-2\,[(40.0)^2+(43.3)^2]/(20.0)^2\} = 2.85\times10^{-8}\,, \qquad (17)$$

is negligible in comparison to that of the near-forward transmitted rays. It should be stressed that Figs.1b,2b show the near-forward scattered intensity alone. In experimental situations, the far-zone beam fields must be added to the near-forward scattered fields to produce the total observed fields [5-8].

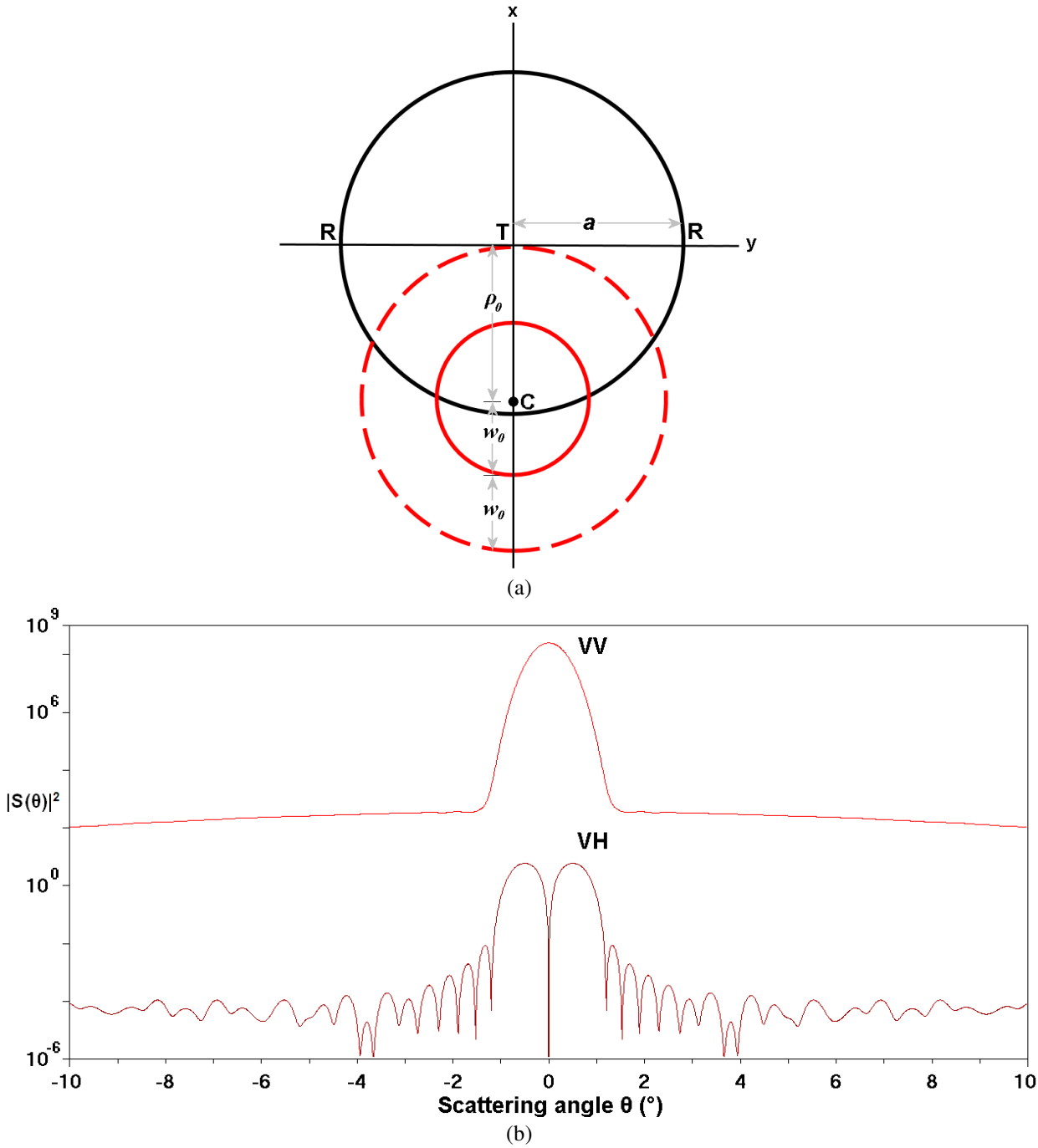

Fig.2. (a) A Gaussian beam of electric field half-width w_0 incident off-axis perpendicular to the horizontal scattering plane at ρ_0, φ_0=180° on a spherical particle of radius a. The center of the beam is at C. Near-forward transmitted rays are incident at T, and near-forward externally reflected rays are incident at R. (b) Near-forward exact GLMT scattered intensity of Eqs.(3a),(3b) as a function of the scattering angle θ in the VV and VH channels for λ=0.5145μm, w_0=20μm, ρ_0=40μm, φ_0=180°, a=43.3μm, M=1.33, and φ=90°.

Although the size of the VV diffracted intensity peak is by definition the same for off-axis incidence in the scattering plane and perpendicular to it (2.28×10^8 in this example), it was noted in [9,10] that the width and shape of the diffraction patterns are very different. This can be understood using three related arguments, each being more detailed and realistic than the preceding one. The first argument is that since the diffracted field is approximately

the Fourier transform of the beam's electric field after being apertured by the particle [3,4], the difference in the diffraction profiles for off-axis incidence in the scattering plane and perpendicular to it can be understood in terms of the size-bandwidth theorem for Fourier transforms. Since the fraction of the beam not obscured along the *y* axis by the sphere in Fig.1a is smaller than the fraction not obscured in the *y* direction tangent to the lower edge of the sphere in Fig.2a, its far-zone diffraction pattern in the *y* direction in Fig.1b should be wider than it is in Fig.2b. Also, since the section through the beam taken in the *y* direction tangent to the lower edge of the sphere in Fig.2a is Gaussian, the diffracted field in Fig.2b should be Gaussian as well.

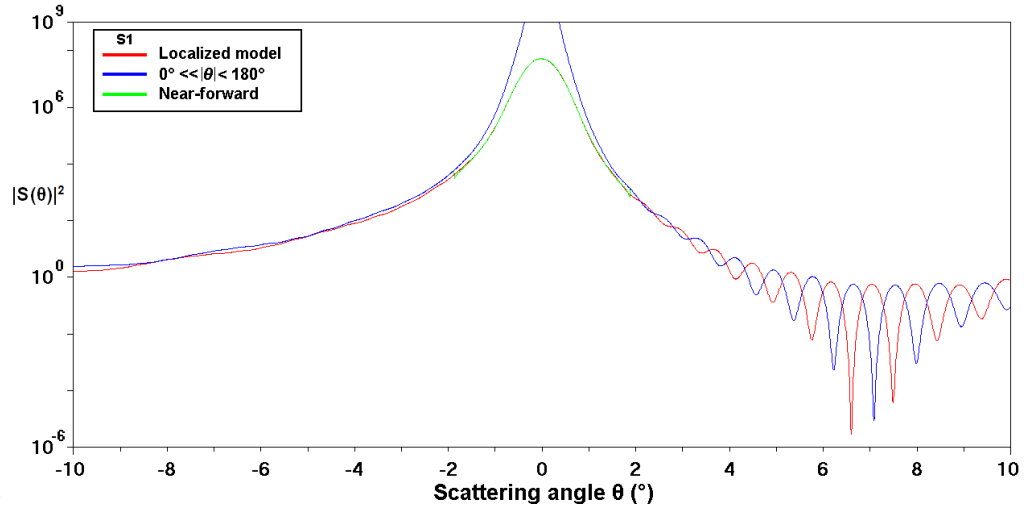

Fig.3. Near-forward exact GLMT VV scattered intensity of Fig.1b as a function of the scattering angle θ for off-axis incidence in the scattering plane, along the approximation of Eqs.(11),(13a)-(13c) for $0°\leq|\theta|\leq 2°$ and the approximation of Eq.(5) for $2°\leq|\theta|\leq 10°$.

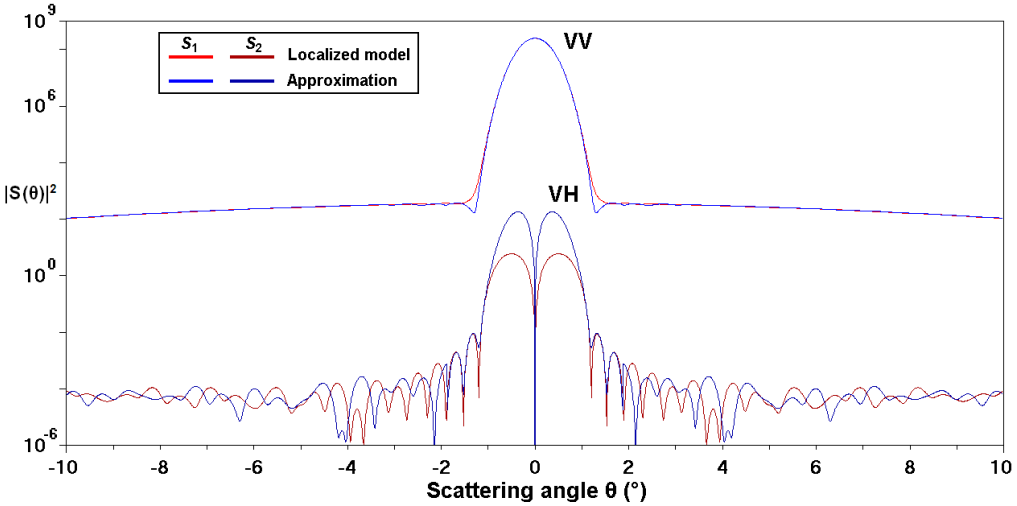

Fig.4. Near-forward exact GLMT VV and VH scattered intensity of Fig.2b as a function of the scattering angle θ for off-axis incidence perpendicular to the scattering plane, along with the approximation of Eqs.(11),(14a)-(14c) for $0°\leq|\theta|\leq 2°$ and the approximation of Eqs.(8),(9a) for $2°\leq|\theta|\leq 10°$.

Figure 3 shows the near-forward scattered VV intensity of Fig.1b for off-axis incidence in the scattering plane along with the small-angle transitional approximation of Eq.(11) for $0°\leq|\theta|\leq 2°$ and the large-angle transitional

approximation of Eq.(5) for $2° \le |\theta| \le 10°$. The large-angle approximation was not considered for angles smaller than 2° because it diverges as $\theta \to 0°$. Similarly, the small-angle approximation was not considered for angles larger than 2° because the computer subroutine we used for the Bessel function of a complex argument was found to become unstable for arguments larger in magnitude than 20, which for our example corresponds to $|\theta| \ge 2.24°$ for the highest included partial wave. Figure 4 shows the near-forward scattered VV and VH intensity of Fig.2b for off-axis incidence perpendicular to the scattering plane along with the two approximations with the same crossover point of $\theta = 2°$, using Eqs.(8),(9a) rather than Eq.(5) for the large-angle approximation. In each of the two cases the two approximations fit the general magnitude of the VV scattered intensity quite well, and they also do a reasonable job reproducing the basic structure of the much weaker VH scattered intensity. But the interference structure of the p=0,1 terms of the Debye series in Fig.3 is rendered 180° out of phase with respect to that of the exact GLMT intensity. This will be commented on in depth in Sec.5.

In order to understand the shape of the diffraction peak on a more quantitative level, we define diffraction of the incident beam by the sphere to be the portion of the scattering amplitudes that is independent of the sphere's composition (see pp.209-210 of [11], and [12]). In the context of the Debye series expansion of the partial wave scattering amplitudes [13-17], this corresponds to $a_n = b_n = 1/2$, which are then substituted into the near-forward approximation to the GLMT scattered electric field of Eqs.(11),(12). We then obtain

$$E_{VV}^{diffracted}(\theta,\varphi;\rho_0,\varphi_0) = E_{HH}^{diffracted}(\theta,\varphi;\rho_0,\varphi_0) \approx [iE_0/(kr)] \sum_{n=1}^{\infty} F_n \, (n+1/2) \, J_0(A_n) \qquad (18a)$$

$$E_{VH}^{diffracted}(\theta,\varphi;\rho_0,\varphi_0) = E_{HV}^{diffracted}(\theta,\varphi;\rho_0,\varphi_0) = 0 \ . \qquad (18b)$$

Equation (18b) suggests that diffraction is polarization-preserving, and thus will not contribute to the cross-polarized intensity observed in Fig.2b. This is not unexpected since diffraction of a plane wave by a straight-edge obstacle is also polarization-preserving when the incident wave is polarized either parallel or perpendicular to the edge (see Sec.11.5 of [18]). An alternate but equivalent interpretation of diffraction is given in [4]. In the appendix of [2] it was shown that when the van de Hulst localization principle (see pp.208-209 of [11]) is applied to Eq.(18a) for a large particle, $2\pi a/\lambda \gg 1$, to approximately convert the sum over partial waves n into an integral over the impact parameter $k\rho'$ via $(n+1/2) \to k\rho'$, the result is identical to Fraunhofer diffraction of a Gaussian beam by a circular obstacle of radius a,

$$E^{diffracted}(r,\theta,\varphi;\rho_0,\varphi_0) = [iE_0/(kr)] \exp(ikz) \exp(-\rho_0^2/w_0^2) \times \int_{k\rho'=0}^{ka} (k\rho') \, d(k\rho') \exp[-s^2 \, (k\rho')^2] \, J_0(A) \ , \qquad (19)$$

where

$$A = (k\rho') \, [\theta^2 - \varepsilon^2 + 2\mathrm{i} \, \theta\varepsilon \cos(\chi)]^{1/2} \quad . \tag{20}$$

The second argument motivating our understanding of the structure of the diffracted intensity of Figs.1b,2b considers a sequence of diffraction geometries for which the obstacle has a straight-edge, rather than the curved edge implicit in Eq.(19). Let the electric field of an incident on-axis beam be

$$E(\rho,\varphi) = E_0 \exp(-\rho^2/w_0^2) \tag{21}$$

in the z=0 plane that contains the obstacle. (i) If the obstacle is absent, the beam of Eq.(21) freely diffracts to the far-zone where it impinges on a viewing screen. The far-zone diffracted field in this case is proportional to the Fourier transform of the incident field, as it was in Eq.(19) for the curved aperture. The diffracted beam is given by

$$E^{diffracted}(r,\theta,\varphi) = [K/(2s^2)] \exp[-\theta^2/(4s^2)] \tag{22}$$

where

$$K \equiv [\mathrm{i}E_0/(kr)] \exp(\mathrm{i}kr) \quad . \tag{23}$$

The Fraunhofer diffracted electric field is independent of φ and Gaussian in θ since the incident field is Gaussian in the z=0 plane. (ii) Now let a large obstacle having a straight edge along the horizontal axis of the z=0 plane cover half of the on-axis beam incident on it, and let a detector array be oriented on the horizontal axis of the distant viewing screen, parallel to the straight-edge. The Fourier transform of the semi-circular beam leaving the z=0 plane gives the far-zone diffracted field at the detector array

$$E^{diffracted}(r,\theta) = [K/(4s^2)] \exp[-\theta^2/(4s^2)] \quad . \tag{24}$$

Since half of the beam is uncovered, half of the field strength of the diffracted field remains. (iii) Now let the detector array on the viewing screen be oriented perpendicular to the straight-edge, both above it (+) and below it (-). The far-zone diffraction pattern on the detector array in this perpendicular orientation is

$$E^{diffracted}(r,\theta) = [K/(4s^2)] \, \{\exp[-\theta^2/(4s^2)] \mp \mathrm{i}G(s^2,\theta)\} \tag{25}$$

where

$$G(s^2,\theta) = (2s^2/\pi) \int_0^{\infty} (k\rho') \, (kd\rho') \exp[-s^2 \, (k\rho')^2] \int_0^{\pi} \sin[(k\rho') \, \theta \sin(\varphi')] \, d\varphi' \quad . \tag{26}$$

It should be noted that $G(s^2,\theta)$=0 when θ=0° so that the field of Eq.(25) has the same value in the forward direction as that of Eq.(24). In addition, both the Gaussian and the function G in Eq.(25) are purely real, so that the diffracted intensity is

$$|E^{diffracted}|^2 = \, [|K|^2/(16s^4)] \, \{\exp[-\theta^2/(2s^2)] + G^2(s^2,\theta)\} \quad , \tag{27}$$

both in the illuminated region above the straight-edge and in the shadowed region below it. We conclude from (ii) and (iii) that although half of the original Gaussian beam is transmitted beyond the straight-edge, the far-zone diffraction pattern has a much simpler structure when the detector array on the viewing screen is oriented parallel to the straight-edge than when it is perpendicular to it.

Now let the coordinate axes in the z=0 plane and on the viewing screen remain fixed while both the beam and straight-edge are translated through the vertical distance ρ_0 in the z=0 plane, perpendicular to the horizontal direction of the straight-edge. (iv) If a detector array on the viewing screen is oriented parallel to the horizontal straight-edge as in (ii), the diffracted field at the detector array is again given by Eq.(24). Nothing has changed since the semi-circular beam leaving the z=0 plane has been translated perpendicular to the horizontal detector array. (v) But if the detector array is now oriented perpendicular to the horizontal straight-edge as in (iii), the diffracted field is

$$E^{diffracted}(r,\theta) = [K/(4s^2)]\ \{\exp[-\theta^2/(4s^2)] \mp iG(s^2,\theta)\}\ \exp(ik\rho_0)\ . \qquad (28)$$

Since the beam and straight-edge have been translated in the direction of the detector array, the Fourier transform of the initial field distribution acquires the translation phase term $\exp(ik\rho_0)$. The diffracted intensity continues to be given by Eq.(27).

These five examples provide an analogy to the problem of current interest since the geometry of (iv) is analogous to that of Fig.2a, with the edge in question being the curved edge of the sphere rather than a straight-edge, and the detector array in the scattering plane oriented in the y direction. Similarly, the geometry of (v) is analogous to that of Fig.1a with the detector array again oriented in the y direction. Since ρ_0=40μm and a=43.3μm, roughly half of the incident beam is cut off by the spherical particle, as in the straight-edge cases (ii)-(v) discussed above. According to Eq.(24) for cases (ii,iv), if exactly half of the incoming beam was cut off by the straight-edge, the intensity at the diffraction maximum of Eq.(24) would be

$$I^{diffracted}(0) = 1/(16s^4) = 2.235\times10^8\ . \qquad (29)$$

The intensity of the diffraction maximum in Figs.1b,2b is 2.28×10^8, which is larger than the prediction of Eq.(29) by 2.0%. The predicted diffracted intensity in Eq.(24) for cases (ii,iv) is parabolic when graphed semi-logarithmically, and qualitatively fits the diffraction peak of Fig.2b quite well. In addition, an analog to the $G^2(s^2,\theta)$ term in Eq.(27) for cases (iii,v) should broaden the diffractive peak for the geometry of Fig.1a with respect to that of Fig.2a.

The third argument for understanding the structure of the diffracted intensity considers the integral of Eq.(19) itself which describes a circular aperture, or a circular obstacle via Babinet's principle, rather than for the straight-edge discussed in the previous paragraphs. By performing successive integration by parts, the integral can be evaluated analytically to give an infinite series of contributions [19,20]. One version of the result is appropriate for $w_0<a$ where the beam is narrow and the circular aperture is wide, so that the aperture cuts off the outer portion of the beam. The other version is appropriate for $w_0>a$ where the beam is wide and the circular aperture is narrow, so that the small portion of the beam passed through the aperture resembles a plane wave with small amplitude and phase distortions. For the $w_0<a$ case of interest here, let

$$\theta' = \theta/\varepsilon \tag{30}$$

be the near-forward scattering angle expressed in terms of multiples of ε of Eq.(4d). Then for a Gaussian beam incident off-axis with φ_0=180° perpendicular to the φ=±90° and θ≥0° scattering plane as in Figs.2a,2b, Eq.(19) simplifies to

$$E^{diffracted}(r,\theta,\varphi=\pm 90°) = [K/(2s^2)]\ \{\exp[-\theta^2/(4s^2)]$$

$$-\exp[-(\rho_0^2+a^2)/w_0^2] \sum_{n=0}^{\infty} [(\rho_0/a)\ (1-\theta'^2)^{1/2}]^n\ I_n[2\rho_0 a(1-\theta'^2)^{1/2}/w_0^2]\}\ . \tag{31}$$

The first term of Eq.(31) is the diffraction pattern of complete beam of Eq.(22) in order to accommodate the on-axis $\rho_0\rightarrow 0$ limit of Eq.(19). Since roughly half of the incident beam in Fig.2a with ρ_0=40μm is cut off by the sphere with a=43.3μm, the infinite series of modified Bessel functions in the second line of (31) should add up to be roughly half of the first term in order to qualitatively resemble Eq.(24) for the straight-edge geometry of cases (ii,iv). The extra complication provided by modified Bessel functions is due to the fact that the edge of the particle projected into the z=0 plane is circular rather than straight.

For a Gaussian beam incident off-axis with φ_0=-90° in the φ=±90° and θ≥0°scattering plane, the integral of Eq.(19) simplifies to

$$E^{diffracted}(r,\theta,\varphi=90°) = [K/(2s^2)]\ \{\exp[-\theta^2/(4s^2)]\ \exp(\mp i k\rho_0)$$

$$-\exp[-(\rho_0^2+a^2)/w_0^2] \sum_{n=0}^{\infty} [\rho_0(1\pm i\theta')/a]^n\ I_n[2\rho_0 a(1\pm i\theta')/w_0^2]\}\ . \tag{32}$$

The infinite series of modified Bessel functions in Eq.(32) should qualitatively resemble the $\mp$ i$G(s^2,\theta)$ term for the straight-edge obstacle of Eq.(25) for cases (iii,v), multiplied by the translation phase factor exp(i$k\rho_0$).

4. Debye Series Decomposition of the Co-Polarized and Cross-Polarized Scattering Amplitudes

The TM and TE Lorenz-Mie partial wave scattering amplitudes a_n and b_n, respectively, can be exactly decomposed into an infinite series of terms, called the Debye series [13-17], which in the short wavelength limit, $2\pi a/\lambda \gg 1$, can be interpreted as diffraction of the partial wave n, external reflection, transmission, and transmission following p-1 internal reflections with p≥1. In order to guarantee convergence in the $n\rightarrow\infty$ limit, diffraction and external reflection are combined together as the p=0 term of the series. The Debye series for VV scattering for a Gaussian beam incident off-axis in the scattering plane has previously been computed and analyzed [21,22], and need not be considered further here. Rather, in this section we focus on VV, VH, HV, and HH scattering for a Gaussian beam incident off-axis perpendicular to the scattering plane. Figure 5 shows the p=0,1,2,3 Debye series terms replacing the complete a_n and b_n in the exact GLMT scattered intensity, in each of the four polarization channels in the φ=90° scattering plane. The beam has λ=0.5145μm, w_0=20μm, ρ_0=40μm, φ_0=180° and the particle has a=43.3μm, M=1.33. For comparison, Fig.5 also repeats the exact GLMT results of Figs.4,5 of [1] which use the complete partial wave scattering amplitudes a_n and b_n .

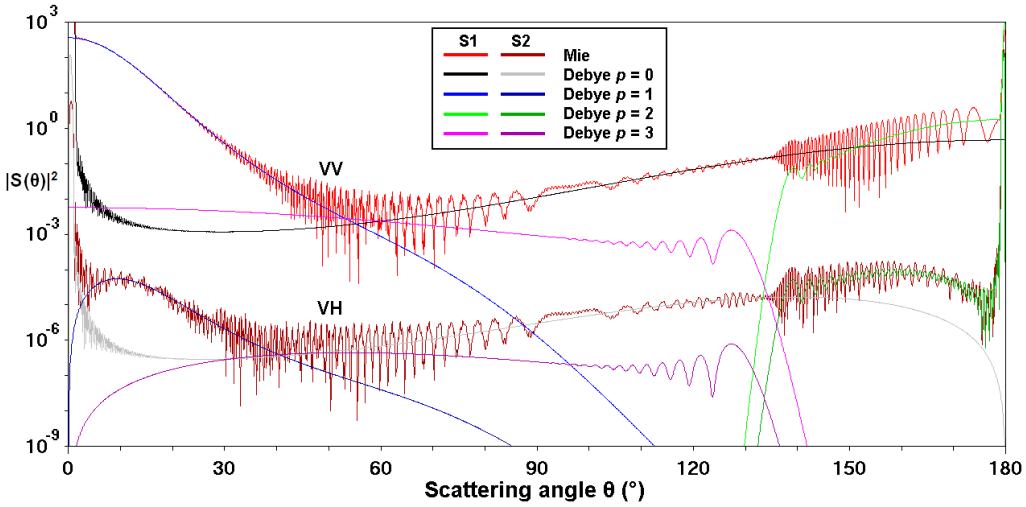

(a)

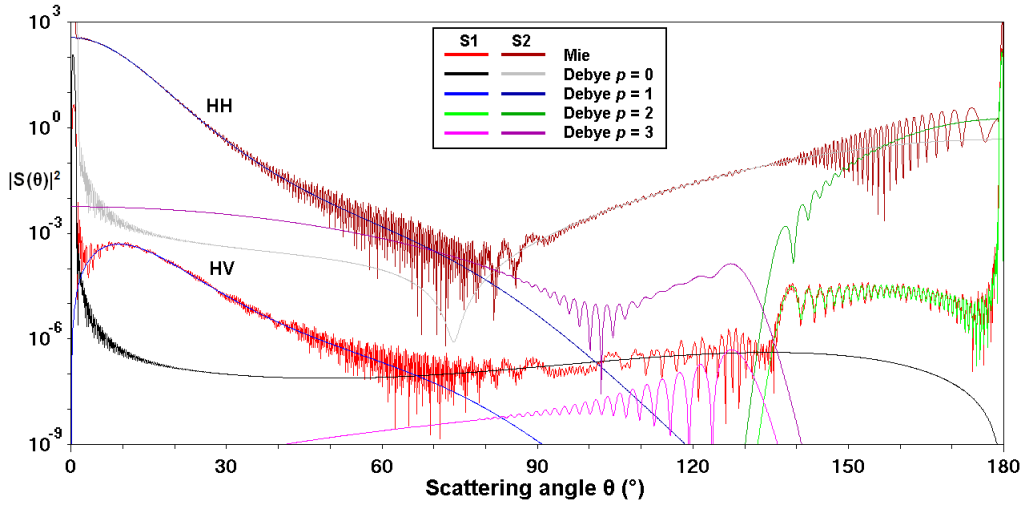

(b)

Fig.5. Exact GLMT VV, VH, HV, HH scattered intensity as a function of the scattering angle θ of Figs.4,5 of [1], and the p=0,1,2,3 terms of the Debye series decomposition of the scattering amplitudes.

As was seen in Sec.3, both the VV and HH intensities are dominated diffraction for $0°<\theta<1°$. They are then dominated by transmission for $1°<\theta<40°$. At this point external reflection, transmission, and scattering with two internal reflections (p=3) become comparable in strength, causing a complicated high-frequency interference pattern for $40°<\theta<90°$. In the HH channel, the role of external reflection is reduced near the Brewster angle dip occurring at θ^B_0=73.9° in ray theory. External reflection then dominates for $90°<\theta<140°$, at which point the contribution of one internal reflection (p=2) becomes comparable in magnitude to external reflection. This produces another high-frequency interference pattern that continues and gradually widens as it enters the glory region, θ~180°. The progression of dominant terms is the same for VH scattering. But for HV scattering, the p=3 Debye term is too small at $\theta\approx60°$ to interfere with external reflection and transmission. Rather, the p=3 term interferes with external reflection in the vicinity of the second order rainbow occurring at θ^R_3=129.9° in ray theory.

Equations (10a),(10b) approximately relate the VH and HV scattering amplitudes to the VV and HH amplitudes for $0°\ll\theta\ll180°$. It was seen in Sec.3 and in [2] that for the example considered here, "much less than" means "to within about 1° of". Thus for θ reasonably close to 0°, both $|S_{VH}|^2$ and $|S_{HV}|^2$ should be approximately given by $\varepsilon^2|S_{VV} - S_{HH}|^2/\sin^2(\theta)$, and thus should be approximately equal to each other. Similarly, for θ reasonably close to 180°, both $|S_{VH}|^2$ and $|S_{HV}|^2$ should be approximately given by $\varepsilon^2|S_{VV}+ S_{HH}|^2/\sin^2(\theta)$, and thus should again be approximately equal to each other. Inspection of Fig.5 shows that this is roughly the case. At θ=90°, Eqs.(10a),(10b) predict that $|S_{VH}|^2\approx\varepsilon^2|S_{VV}|^2$, and $|S_{VH}|^2\approx\varepsilon^2|S_{HH}|^2$. Inspection of Figure 5 shows that at θ=90° and for p=0,3, $|S_{VH}|^2\approx2.5\times10^{-4}|S_{VV}|^2$. Similarly, for p=0,1,3, $|S_{HV}|^2\approx2.5\times10^{-4}|S_{HH}|^2$. This is in reasonable agreement with $\varepsilon^2=2.68\times10^{-4}$ for this example. These results confirm the approximate validity of Eqs.(10a),(10b). They also explain why the TE p=2 rainbow appears prominently in both the VH and HV intensities of Fig.5. The p=2 rainbow occurs at θ^R_2=137.5° in ray theory. In Fig.5 the $|S_{VV}|^2$ intensity is about 10^{-1} at θ^R_2, whereas the$|S_{HH}|^2$ intensity is about10^{-3} there. This difference in strength is due to two effects. (i) The principal rainbow peak is absent for the TM polarization [16,23], thus suppressing the strength of the TM rainbow relative to that of the TE rainbow. (ii) As is seen in Fig.2a and Eqs.(16,17), rays incident in the scattering plane with $y\approx0$ near the center of the sphere are much stronger than rays incident at $y\approx\pm a$ due to the Gaussian falloff of the incident beam. As y increases, the scattering angle of the p=2 rays decreases from θ=180° to the Descartes rainbow angle at θ^R_2=137.5°. Near the rainbow angle these rays are called lower supernumerary rays. As y continues to increase, the scattering angle of the rays then increases to the critical angle θ^C_2=165.0° for grazing incidence. These rays are called upper supernumerary rays. The strength of the rays continually decreases during this progression. This effect serves to weaken the p=2 upper supernumerary rays with respect to the lower supernumerary rays, thus more rapidly damping out the supernumerary interference pattern. It also is the cause of the continuous rise in p=2 scattering as $\theta\rightarrow180°$. Since $|S_{VV}|^2\approx10^{-1}$ and $|S_{HH}|^2\approx10^{-3}$ at the p=2 rainbow and $\cos(\theta^R_2)$=-0.737, Eqs.(10a),(10b) predict that the S_{VV} contribution to both VH and HV scattering will dominate over the S_{HH} contribution in the vicinity of the p=2 rainbow.

Figure 7a of [21] where $2\pi a/\lambda$=529 and Fig.2a of [25] where $2\pi a/\lambda$=100 show that for plane wave incidence, the p=0 external reflection intensity decreases only very slowly from $\theta\approx0°$ to θ=180°. But for VV, VH, HV, and HH scattering in Fig.5 where $2\pi a/\lambda$=529, the external reflection intensity increases as a function of θ and dominates the scattering for $90°<\theta<140°$. This can be explained by the fact the incident rays in Fig.2a increase in strength from $y\approx\pm a$, corresponding to $\theta\approx0°$, to $y\approx0$, corresponding to $\theta\approx180°$. The p=1 contribution in Fig.5 to VV scattering is nearly equal to that of HH scattering, and is similar to the monotonic decrease of the p=1 contribution for plane wave incidence in Fig.7a of [21] and Fig.2b of [24]. Similarly, the p=1 contribution to VH scattering in Fig.5 is nearly equal to that of HV scattering, and goes to zero as $\theta\rightarrow0°$, as was shown in [2]. In ray theory, grazing incident rays are transmitted with zero intensity at the critical scattering angle θ^C_1=82.5°. In wave theory, the scattered intensity continues beyond this angle due the Fock transition to electromagnetic surface waves [15]. The surface wave contribution is evident in Fig.5 for θ>82.5°. The rate of falloff is roughly linear in the semi-logarithmic figure, indicating that the surface wave attenuation is roughly exponential, as it was for plane wave incidence. Since the strength of the incident rays decreases from $y\approx0$ to $y\approx\pm a$ as the scattering angle decreases from θ=0° to θ^C_1, the p=1

intensity for off-axis incidence perpendicular to the scattering plane should fall off faster than it does for plane wave incidence.

As mentioned above, the major difference of the p=2 TM rainbow from the TE rainbow for both plane wave and off-axis Gaussian beam incidence perpendicular to the scattering plane is the suppression of the principal rainbow peak due to the fact that the TE rainbow scattering amplitude is approximately proportional to the Airy function Ai(x), while the TM rainbow scattering amplitude is approximately proportional to a linear combination of Ai(x) and its derivative [16,23], Ai′(x). However, the difference of the p=3 TM rainbow in the HH scattering channel in Fig.5 from the TE rainbow in the VV scattering channel is more substantial, and is similar to the differences encountered in p=3 scattering of a plane wave, as seen in Fig.11 of [24]. The p=3 rainbow in the HH channel is almost devoid of supernumeraries for 110°<θ<125°, and has a low-amplitude, strong-contrast interference pattern for 95°<θ<105°. This behavior may be understood as follows. As rays are incident in the horizontal scattering plane from the sphere center y≈0 to its edge y≈a, the p=3 deflection angle Θ (scattering angle θ in parentheses) starts at Θ=360° (θ=0°). It then decreases (increases) to the Descartes rainbow angle Θ^R_3=230.1° (θ^R_3=129.9°). The deflection (scattering) angle then increases (decreases) to the critical angle Θ^C_3=247.5° (θ^C_3=112.5°) for grazing incidence. Electromagnetic surface waves begin at this point, continue the role played by the upper supernumerary rays to larger Θ (smaller θ), and exponentially decrease as a function of Θ (increase as a function of θ). At the same time, the incident rays associated with the Gaussian beam progressively decreases in strength from the value given in Eq.(16) to the value given in Eq.(17). This causes the p=3 scattered intensity to also decrease as a function of θ, with the partial focusing associated with the p=3 rainbow temporarily boosting the scattered intensity back up before it continues to decrease again. Since the internal reflection Brewster angle for p=3 scattering occurs for θ^B=115.5° in ray theory, the strength of the lower supernumerary rays near this angle and having impact parameter b≡sin(θ_i)~0.80 are greatly suppressed with respect to that of the upper supernumerary rays, severely reducing the bright-to-dark contrast of the supernumerary interference pattern. The oscillatory structure of p=3 HH intensity in Fig.5 for 95°<θ<105° is due to interference of the nearly equal contributions of (i) electromagnetic surface waves that grow in strength as a function of θ as they approach θ^C_3, with (ii) lower supernumerary rays of smaller impact parameters (e.g. b~0.70) that decrease in strength as a function of θ due to a combination of (a) the decreasing strength of the incident Gaussian rays and (b) the approach to the Brewster angle region.

5. Time-Domain Analysis of Co-Polarized and Cross-Polarized Scattering

In time-domain scattering, an electromagnetic pulse is incident on the sphere, rather than a plane wave or a transversely localized beam of infinite temporal extent. In this section we take the pulse to be both spatially and temporally Gaussian. Its electric and magnetic field have a transverse half-width w_0 and a temporal half-width σ/c. Its frequency spectrum is centered on the wavelength λ_0 whose associated wave-number is k_0=2π/λ_0. When a spatially Gaussian beam of wave-number k is incident on the sphere, we denote the scattered field by $E^{GLMT}(k,\theta)$. Then for an incident pulse containing a spectrum of wave-numbers, the scattered electric field is the GLMT response of the single wave-number k integrated over the spectrum of the beam [25-31],

$$E_{scattered}(t,\theta) = [E_0\sigma/(2\pi^{1/2})] \int_{-\infty}^{\infty} dk\, E^{GLMT}(k,\theta)\, \exp[-(k-k_0)^2\sigma^2/4]\, \exp(-ickt)\ . \qquad (33)$$

Light scattered via certain physical processes, such as transmission, has a relatively short path length inside the sphere and exits it soon after the pulse's arrival. On the other hand, light scattered via other physical processes, such as transmission following a number of internal reflections, has a relatively long path length inside the sphere and exits it long after the pulse's arrival. In this way time-domain scattering displays the unique signature of each physical process contributing to scattering without having to explicitly calculate the terms of the Debye series.

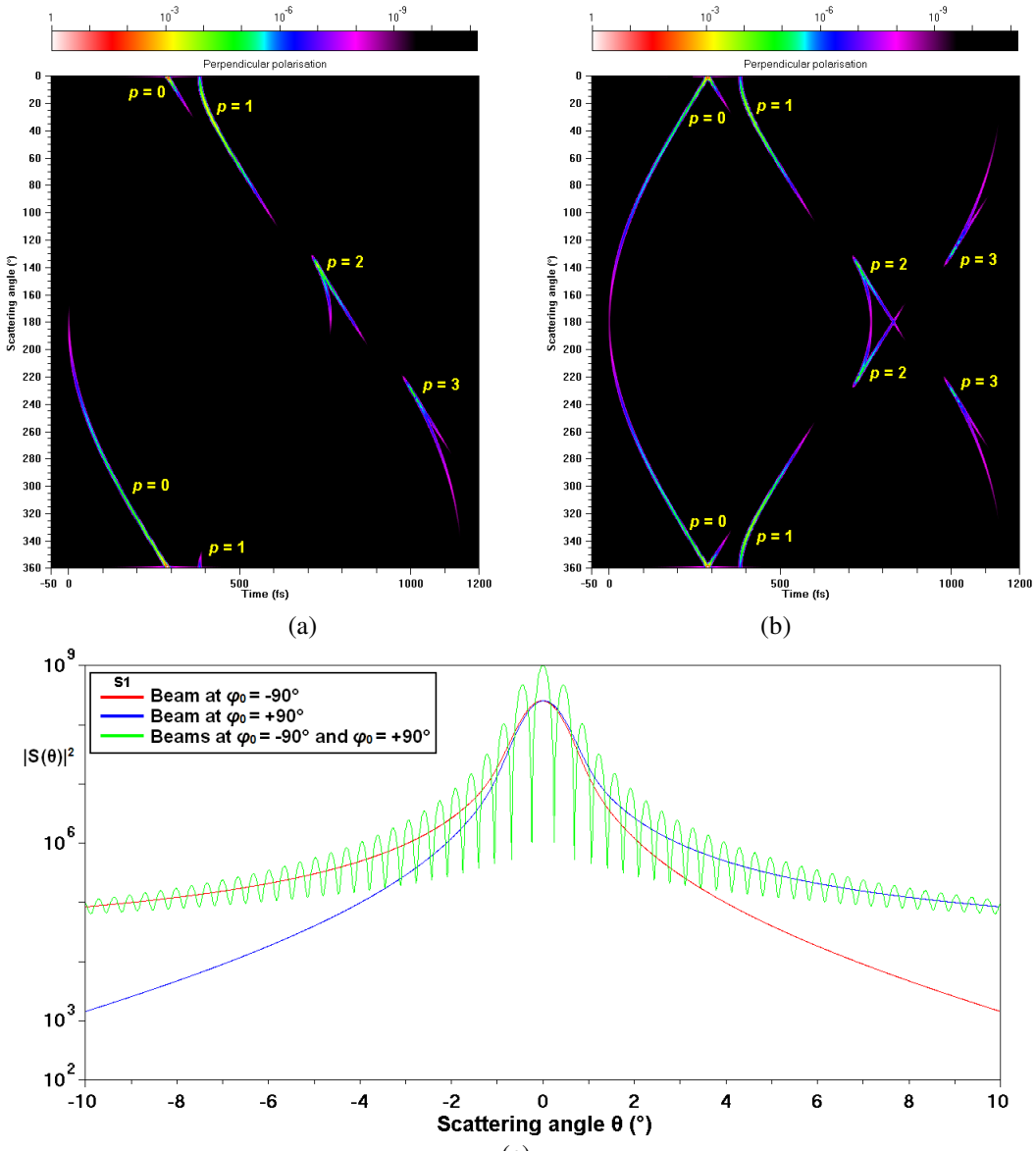

Fig.6. Time-domain scattered intensity as a function of the scattering angle θ and time delay t of the exact VV scattering amplitude for a Gaussian pulse with λ_0=0.5145μm, σ/c=3.00fs, and w_0=20μm by a spherical particle with a=43.3μm, M=1.33. (a) The pulse is translated off-axis with ρ_0=40μm, φ_0=-90° in the φ=90° scattering plane. (b) A pair of coherent identical pulses are symmetrically translated off-axis with ρ_0=40μm, φ_0=±90° in the φ=90° scattering plane. (c) Intensity of the p=0 Debye term as a function of the scattering angle θ for the beam with (i) ρ_0=40μm, φ_0=-90°, (ii) ρ_0=40μm, φ_0=90°, and (iii) the interference pattern for p=0 scattering when both beams are present.

Figure 6a shows the time-domain graph of the exact GLMT scattering amplitude of Eq.(3a) for the VV polarization channel for a Gaussian pulse with λ_0=0.5145μm, w_0=20μm incident on a spherical particle with a=43.3μm, M=1.33. The temporal characteristics of the pulse are σ/c=3.00fs, giving a temporal full-width-at-half-maximum of the electric field of 5.0fs. In the Fourier transform in Eq.(33), the wavelength range integrated over is 0.348μm≤λ≤0.985μm, corresponding to truncating the incident Gaussian intensity at -60dB. The pulse is translated off-axis with ρ_0=40μm, φ_0=-90° in the φ=90° scattering plane. The integral in Eq.(33) was evaluated using a 2^{13}=8,192 point Fast Fourier Transform (FFT), the details of which are given in the Appendix. The graph, with an angular resolution of $\Delta\theta$=1°, shows the signature of the p=0,1,2,3 Debye series processes. The graph is similar to that for scattering by a plane wave pulse having similar parameters, as shown in Fig.5 of [29], except that (i) the angular range of Fig.6a is unfolded to 0°≤θ≤360°, compared to the 0°≤θ≤180° angular range of Fig.5 of [29], and (ii) Fig.6a does not show the trajectories of rays incident with y>0 in Fig.1a because they are suppressed by the Gaussian falloff of the beam.

Only one arm of the inverted-V signature of diffraction is present in Fig.6a at θ≈0°, t≈289fs due to light deflected past the y=-a edge of the sphere, whereas both arms are evident for plane wave incidence in Figs.5,6a of [29] due to rays of equal strength deflected past both the y=±a edges. The shape of the external reflection portion of the p=0 signature is symmetric about the location of the axially incident ray at θ=180°, t≈0fs. But the reflected signal becomes progressively weaker for θ<180° and progressively stronger for θ>180° due to the strength of the rays of the incident Gaussian beam becoming weaker for y>0 and stronger for y<0. The single arm of the diffraction portion of the p=0 signature for θ≥0°, t≈289fs is the continuation of p=0 external reflection for θ≤360°. Similarly, the shape of the p=1 signature is symmetric about the location of the axial ray at θ=0°, t=384fs. But again the transmitted signal becomes progressively weaker for θ<0° (i.e. θ<360° in the figure) and progressively stronger for θ>0° due to the Gaussian falloff of the strength of the incident rays. The small portion of the p=1 signature for θ≤360°, t≈384fs is the continuation of the p=1 signature for θ≥0°. The inverted curving-V signals of the p=2,3 rainbows are also evident.

In order to validate our interpretation of the p=0,1,2,3 structures in Fig.6a, Fig.6b shows the time-domain graph for a pair of identical coherent Gaussian beams with ρ_0=40μm, φ_0=±90° incident on the particle. Whereas the single Gaussian beam of Fig.6a illuminated one side of the particle, the additional beam in Fig.6b now illuminates the other side. In particular, the pair of beams produces both arms of the characteristic inverted-V signature of diffraction by a plane wave, where light is deflected equally at both edges of the particle. Figure 6c shows the intensity of the p=0 Debye term as a function of θ when the first beam alone is present, the second beam alone is present, and when both beams are present. The periodicity of the interference pattern produced when both beams are present corresponds to the interference of two effective point sources spaced by d=84.8±0.7μm. This is comparable to the particle diameter of 86.6μm, and can be interpreted as the combination of diffraction and external reflection at the two opposite edges of the particle being the two effective point sources of the interference pattern.

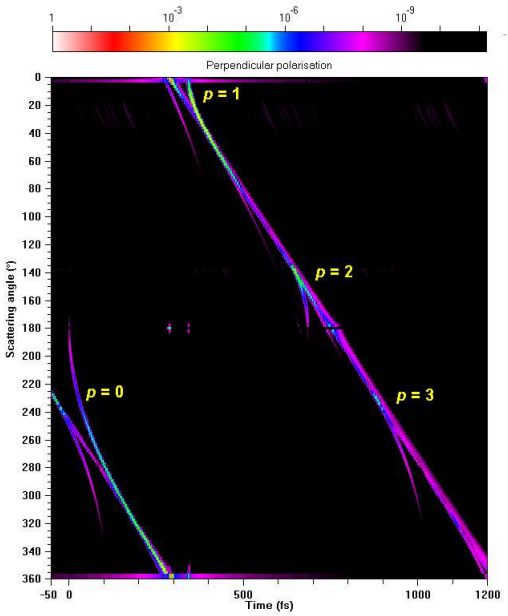

Fig.7. Time-domain scattered intensity as a function of the scattering angle θ and time delay t of the approximation of Eqs.(5),(11) for the same pulse and particle as Fig.6.

For comparison to Fig.6a, Fig.7 shows the time-domain graph of the approximation of Eqs.(5),(11) in the VV scattering channel for the same Gaussian pulse translated off-axis in the scattering plane, with $\Delta\theta$=2°, and using a 2^{17}=131,072 point FFT to reduce the noise level and aliasing in the graph. The computer run time to produce Fig.7 was 18h using an Intel i7 processor running at 3.8GHz in "turbo-mode". Although the time delay matches that of Fig.6a for the p=0 signature, an echo of the p=3 rainbow signal is superimposed on it. The p=1,2,3 signals have the correct shape, but their time delay is shifted, and they are joined together rather than being distinct as in Fig.6a. At least three echoes of the p=1,2,3 structure occur with decreasing intensity at time delays in multiples of Δt=295.03±0.18fs for larger t, and at least one occurs for smaller t. The reason for this artifact is not presently understood.

The problematical comparison between the approximation of Eqs.(5),(11) and the exact GLMT result for time-domain scattering occurs in spite of the good fit of the approximation to the overall magnitude of the exact GLMT intensity in the frequency-domain, as illustrated in Fig.1b here and Fig.1 of [2]. We believe the reason for the problematical comparison is as follows. The Fourier transform in Eq.(33) interrogates oscillations of the scattering amplitude with 2^{17} reference spatial frequencies in order to precisely determine the phase of each component, and thus to determine its location on the time-domain graph. As was seen in Sec.4, the high-frequency oscillations in the exact GLMT intensity are caused by the interference of two or more Debye series processes of comparable magnitude. It was seen in Figs.1-6 of [2] that the phase of these oscillations for our approximation drifted with respect to the phase for the exact GLMT intensity. Our approximation was based on the asymptotic approximation of the associated Legendre functions $P_n^m[\cos(\theta)]$, and the GLMT angular functions $\pi_n^m(\theta)$ and $\tau_n^m(\theta)$ derived from them. This asymptotic approximation was valid for $0° \ll \theta \ll 180°$ and $n \gg 1$ in order to avoid the Bessel-function-like focusing behavior in the $\theta \approx 0°$, 180° regions, and to ensure that there are a large number of undistorted oscillations of the functions in the angular region between the two focusing regions, respectively. It was seen in Sec.4 that

scattering into the first half of the forward hemisphere and the last half of the backward hemisphere is frequently due to paraxial rays. Using the van de Hulst localization principle as a qualitative guide, such rays are expected to correspond to relatively low partial waves, where the asymptotic approximation to $P_n^m[\cos(\theta)]$ is not valid. So when a particular high-frequency oscillation in the intensity is caused by a Debye series term dominated by large n interfering with another Debye series term, such as p=0,1 in an angular region where it is dominated by small n, it is quite likely that our $n \gg 1$ approximation will not render the phase of the interference oscillation correctly. Prime examples of this are the p=0,1 interference in Fig.3 for $4° \leq \theta \leq 10°$, and the interference of p=0 external reflection with the principal peak of the p=3 rainbow in Fig.1 of [2]. We had noted in [2] that our approximation contains an infinite series of terms of order (T), (T/n), and smaller. Only the first one or two terms of the series were used in obtaining Figs.3,4 here and Figs.1-6 of [2]. Including additional smaller terms of this series will not help resolve the phase drift of our approximation since all the terms in the series are derived from the $n \gg 1$asymptotic approximation of $P_n^m[\cos(\theta)]$. This appears to be a fundamental limitation of our approximation. But it should be of only minor consequence if the detector array used in scattering experiments is sufficiently coarse so as to not resolve individual high-frequency intensity oscillations.

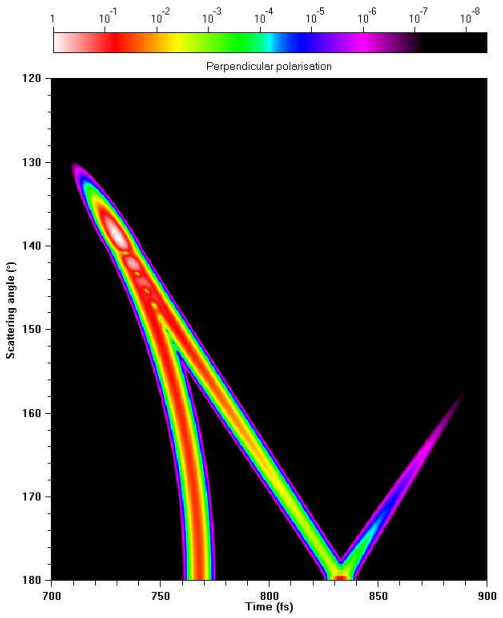

Fig.8. Time-domain scattered intensity as a function of the scattering angle θ and time delay t of the VV Lorenz-Mie scattering amplitude for a plane wave pulse with λ_0=0.5145μm, σ/c=3.00fs by a spherical particle with a=43.3 μm, M=1.33.

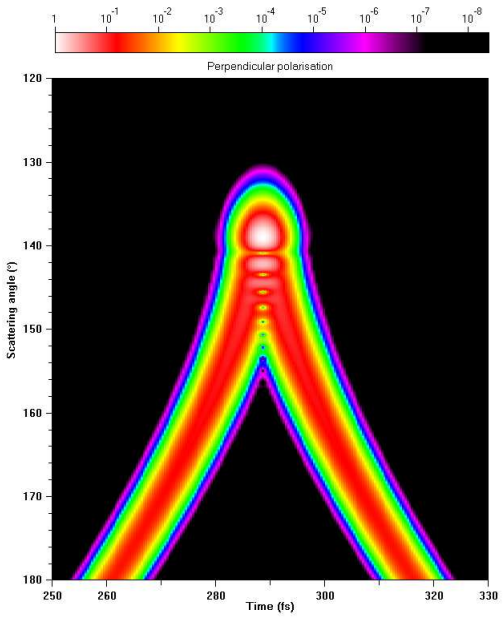

Fig.9. Time-domain scattered intensity as a function of the scattering angle θ and time delay t of the VV Airy theory scattering amplitude for the same plane wave pulse and sphere as Fig.8.

This problematical comparison for time-domain scattering is an example of the importance of phase information in signals, which was stressed in a general context in [32]. In order to validate this conjecture, we computed p=2 scattering of an x-polarized temporally Gaussian and spatially plane wave pulse with λ_0=0.5145μm, σ/c=3.00fs by a spherical particle with a=43.3μm, M=1.33, giving a size parameter of $2\pi a/\lambda$=529. The integral of Eq.(33) was evaluated using a 2^{13}=8,192 point FFT with only the p=2 portion of the a_n and b_n partial wave scattering amplitudes,

as described in the Appendix. The resulting time-domain graph in the vicinity of the first-order rainbow is shown in Fig.8, and is quite similar to Fig.10 of [29] for slightly different pulse parameters. Time-domain scattering of the same beam by the same sphere was also computed with the exact Lorenz-Mie-Debye scattering response now being replaced by the Airy-theory response. For a sphere of this size, Airy theory gives a close approximation to the p=2 scattered intensity as shown in Fig.3 of [24] where $2\pi a/\lambda$=1,000. The phase of the Airy theory supernumerary interference pattern drifts only very slowly with respect to that of the exact Lorenz-Mie result. But the time-domain graph for Airy theory in Fig.9 exhibits substantial differences from that of Fig.8, even quite close to the rainbow's principal peak. The reason for this is that the two arms of the time-domain signature in Figs.8,9 are the contribution of the two supernumerary rays, whose coalescence produces the principal rainbow maximum in ray theory at $\theta^R_2 \approx 137.5°$, $t \approx 730$fs in Fig.8 and at $t \approx 290$fs in Fig.9. The difference in delay times is inconsequential, and merely reflects different conventions for the start of the delay-time clock. The phase of each of the supernumerary rays is given by

$$\Phi = (4\pi a/\lambda)\,[2M\cos(\theta_t) + 1 - \cos(\theta_i)] + \zeta\,, \tag{34}$$

where θ_i is the angle of incidence of each of the two rays corresponding to the same scattering angle θ given by

$$\theta = 180° + 2\theta_i - 4\theta_t\,, \tag{35}$$

θ_t is the transmitted angle whose value is related to θ_i by Snell's law, and ζ is the non-path length scattering amplitude phase, which is 90° for the lower supernumerary ray and 0° for the upper supernumerary ray (see pp.206-207 of [11]). In Airy theory each of these phases is Taylor series expanded about the Descartes rainbow angle, and only the first two terms of the Taylor series expansion is retained [16]. This provides a good approximation to the rainbow intensity as a function of θ until the scattering angle gets sufficiently far into the supernumerary region. But the phase truncation is seen in Fig.9 to seriously distort the entire time-domain signature as a function of θ and t, producing a symmetric behavior of the two supernumerary rays in Fig.9, rather than the correct asymmetric behavior of Fig.8. This example illustrates the importance of precise phase information for determining ray trajectories in time-domain scattering.

6. Final Thoughts

This study was motivated by the common perception that since cross-polarized scattering cannot occur for an electromagnetic plane wave incident on a single homogeneous spherical particle, it continues to be impossible when the incident beam is transversely localized. We found that this perception is incorrect, and that both co-polarized and cross-polarized scattering occur if an incident focused Gaussian beam is translated off-axis perpendicular to the scattering plane. The question then becomes why does cross-polarized scattering occur for this geometry? For scattering by a spheroid, the intuitive and easily visualized mechanism that produces nonzero cross-polarized scattering is that the plane of incidence of a skew ray changes at each interaction with the spheroid surface. Thus the direction of the components of the electric field perpendicular and parallel to the plane of incidence changes as well [33]. But for scattering by a sphere, the wave theory origins of cross-polarized scattering are less intuitive, and

are instead most easily arrived at using a rather abstract mathematical analysis. Cross-polarized scattering in these situations is due to the combination of circular symmetry breaking in wave theory for off-axis incidence, and the constraints imposed by the requirement that an off-axis electromagnetic beam satisfies Maxwell's equations.

When the Gaussian beam is incident off-axis on the sphere, both the co-polarized and cross-polarized scattering amplitudes contain sums over partial waves and azimuthal modes, whereas scattering of a plane wave or an on-axis Gaussian beam requires only a sum over partial waves. The additional complexity encountered when attempting to deal with the sum over azimuthal modes appears to not necessarily be an inevitable feature of the theory. We devised an accurate approximation to the polarization-resolved scattering amplitudes which consists of an infinite series of contributions, each of which possesses the virtue that the sum over azimuthal modes can be evaluated analytically, both for θ in the near-forward- and near-back-scattering regions, as well as for $0° \ll \theta \ll 180°$. The sum of the contributions for $0° \ll \theta \ll 180°$ was found to be rapidly convergent for large particles and moderately focused beams, with only one or two terms required to produce a close match to the overall magnitude of the exact GLMT polarization-resolved scattered intensity. We further probed the structure of the exact GLMT scattering amplitudes by examining the various terms of their Debye series expansion. We also further probed the structure of the approximation by assessing its accuracy in the time-domain, where precise phase information was found to be as important as precise magnitude information. We found that time-domain scattering accentuated the consequences of the phase drift in the high-frequency intensity oscillations inherent in our approximation. It is hoped that the lessons learned here in the development of this approximation can lead to further developments and simplifications of the GLMT version of electromagnetic scattering of a transversely focused off-axis beam by a spherical particle.

Appendix

The details of the FFT algorithm as used in obtaining Fig.6 are as follows. The angular frequency, ω_0, corresponding to the central wavelength in the spectrum of the pulse, λ_0=0.5145μm, is $\omega_0=3.66366\times10^{15}\ s^{-1}$. With N=8,192 angular frequencies sampled on a grid of spacing ($\Delta\omega$), we chose ω_0 to be one-quarter of the maximum frequency $N(\Delta\omega)$, or

$$(\Delta\omega) = 4\omega_0/N \ . \qquad \text{(A1)}$$

The grid spacing, (Δt), in the time-domain is then

$$(\Delta t) = 2\pi/[N(\Delta\omega)] = \lambda_0/(4c) = 0.42875 \text{ fs}, \qquad \text{(A2)}$$

which spatially corresponds to one-quarter of the central wavelength. This gives the Nyquist time $t_{Nyquist}=N(\Delta t)/2$, and the first alias time

$$t_{alias} = N(\Delta t) = 3{,}512.32 \text{ fs}. \qquad \text{(A3)}$$

The time delay of the signature of each Debye series process will thus repeat at multiples of $\pm t_{alias}$.

The time delay of the axial ray of the p Debye process with respect to that of the externally reflected axial ray, which is taken to be zero delay time, is

$$t_{axial\ ray} = 2apM/c = 383.9p \text{ fs} \ , \qquad \text{(A4)}$$

and the time delay of the grazing incidence ray is

$$t_{grazing\ incidence\ ray} = 2a/c + 2ap(M^2\text{-}1)^{1/2}/c = (288.7 + 253.1p) \text{ fs}. \qquad \text{(A5)}$$

The signature of the p=1 Debye process extends from 384 fs $\le t \le$ 542 fs, excluding the portion for $t >$ 542 fs due to electromagnetic surface waves. For the p=10 Debye process, Eq.(A4) gives $t_{axial\ ray}$=3,839 fs, which is greater than t_{alias} = 3,512.32 fs for N = 8,192. Consequently, the lower first-alias for p=10 will appear at 327 fs, close to the time-domain signature of the p=1 Debye process. This is also the case for the lower first-alias of $11 \le p \le 15$, where Eq.(A5) gives the lower first-alias time of the grazing incidence ray as 573 fs. In order to prevent Fig.6 from being contaminated by aliases of high-p processes, we computed the time delay signature of the $0 \le p \le 3$ processes individually, and then composited them together. Since each individual signature has a localized range of time delays, its aliases will not occur in the time delay interval used in the compositing (-50 fs $\le t \le$ 1,200 fs in Fig.6). Alternatively, we could have used a much larger value of N with the entire GLMT response so as to hopefully move the aliases of high-p processes out of the range of the signature of the low-p processes of interest. This strategy was used in Fig.7 where we used N = 131,072 for the time-domain representation of our approximation to the scattering amplitudes. Such large values of N imply very long computation times and computer memory can become an issue, which is why in Fig.7 we used $\Delta\theta$=2°, rather than the $\Delta\theta$=1° as in Fig.6.

Acknowledgment

P.L. and J.A.L. thank Prof. David Cannell of the University of California at Santa Barbara for a series of conversations that led to our investigation of cross-polarized scattering.

References

[1] Lock JA, Laven P. Co-polarized and cross-polarized scattering of an off-axis focused Gaussian beam by a spherical particle. 1. Exact GLMT formalism. JQSRT 2018; 221; 260-272.

[2] Lock JA, Laven P. Co-polarized and cross-polarized scattering of an off-axis focused Gaussian beam by a spherical particle. 2. Sum over azimuthal modes. JQSRT 2018; 221; 273-285.

[3] Heinson WR, Chakrabarti A, Sorensen CM. Crossover from spherical particle Mie scattering to circular aperture diffraction. J Opt Soc Am A 2014;31:2362-4.

[4] Berg MJ, Sorensen CM. A review and reassessment of diffraction, scattering, and shadows in electrodynamics. JQSRT 2018:210:225-39.

[5] Brillouin L. The scattering cross section of spheres for electromagnetic waves. J Appl Phys 1949;20:1110-25.

[6] Hodges JT, Gréhan G, Gouesbet G, Presser C. Forward scattering of a Gaussian beam by a nonabsorbing sphere. Appl Opt 1995;34:2120-32.

[7] Lock JA, Hodges JT. Far-field scattering of a non-Gaussian off-axis axisymmetric laser beam by a spherical particle. Appl Opt 1996;35:6605-16.

[8] Lock JA, Hodges JT. Far-field scattering of an axisymmetric laser beam of arbitrary profile by an on-axis spherical particle. Appl Opt 1996;35:4283-90.

[9] Chevaillier J-P, Fabre J, Hamelin P. Forward scattered light intensities by a sphere located anywhere in a Gaussian beam. Appl Opt 1986;25:1222-5.

[10] Gréhan G, Gouesbet G, Guilloteau F, Chevaillier J-P. Comparison of the diffraction theory and the generalized Lorenz-Mie theory for a sphere arbitrarily located into a laser beam. Opt Comm 1992;90:1-6.

[11] van de Hulst H. Light scattering by small particles. 1981:Dover;New York.

[12] Lock JA, Hovenac EA. Diffraction of a Gaussian beam by a spherical obstacle. Am J Phys 1993;61:698-707.

[13] Debye P. Das elektromagnetische Feld um einen Zylinder und die Theorie des Regenbogens. Phys Zeit 1908;9:775-8, reprinted and translated into English in Marston PL. ed. Geometric aspects of scattering, MS89. 1994:SPIE Press; Bellingham WA.

[14] van der Pol B, Bremmer H. The diffraction of electromagnetic waves from an electrical point source round a finitely conducting sphere, with applications to radiotelegraphy and the theory of the rainbow. Phil Mag 1937;24:825-64.

[15] Nussenzveig HM. High-frequency scattering by a transparent sphere. I. Direct reflection and transmission. J Math Phys 1969;10:82-124.

[16] Nussenzveig HM. High-frequency scattering by a transparent sphere. II. Theory of the rainbow and the glory. J Math Phys 1969;10:125-76.

[17] Lock JA. Cooperative effects among partial waves in Mie scattering. J Opt Soc Am A 1988;5:2032-44.

[18] Born M, Wolf E. Principles of optics, seventh ed. 1999: Cambridge University Press; Cambridge UK.

[19] Olafe GO. Diffraction by Gaussian apertures. J. Opt Soc Am 1970,60:1654-7.

[20] Schell RG, Tyras G. Irradiance from an aperture with a truncated-Gaussian field distribution. J Opt Soc Am 1971;61:31-5.

[21] Lock JA. Contribution of high-order rainbows to the scattering of a Gaussian laser beam by a spherical particle. J Opt Soc Am A 1993;10:693-706.

[22] Jia X, Shen J, Yu H. Calculation of generalized Lorenz-Mie theory based on the localized beam models. JQSRT 2017;195:44-54.

[23] Können GP, de Boer JH. Polarized rainbow. Appl Opt 1979;18:1961-5.

[24] Hovenac EA, Lock JA. Assessing the contributions of surface waves and complex rays to far-field Mie scattering by use of the Debye series. J Opt Soc Am A 1992;9:781-95.

[25] Gouesbet G, Gréhan G. Generic formulation of a generalized Lorenz-Mie theory for a particle illuminated by laser pulses. Part Part Syst Char 2000;17:213-24.

[26] Mees L, Gouesbet G, Gréhan G. Scattering of laser pulses (plane wave and focused Gaussian beam) by spheres. Appl Opt 2001;40:2546-50.

[27] Mees L, Gréhan G, Gouesbet G. Time-resolved scattering diagrams for a sphere illuminated by a plane wave and focused short pulses. Opt Comm 2001;194:59-65.

[28] Laven P. Separating diffraction from scattering: the million-dollar challenge. J Nanophotonics 2010;4,041593.

[29] Laven P. Time domain analysis of scattering by a water droplet. Appl Opt 2011;50:F29-F38.

[30] Lock JA, Laven P. Mie scattering in the time domain. Part I. The role of surface waves. J Opt Soc Am A 2011;28:1086-95.

[31] Lock JA, Laven P. Mie scattering in the time domain. Part II. The role of diffraction. J Opt Soc Am A 2011;28:1096-1106.

[32] Oppenheim AV, Lim JS. The importance of phase in signals. Proc IEEE 1981;69:529-41.

[33] Lock JA. Ray scattering by an arbitrarily-oriented spheroid. II. Transmission and cross-polarization effects. Appl Opt 1996;35:515-31.